PIER C

Design and Evaluation of 5-DOF Magnetic Bearing System for Saucer-Shaped Flywheel Battery

Weiyu Zhang*, An Li, and Jingwen Wang

School of Electrical and Information Engineering, Jiangsu University, Xuefu Road 301, Zhenjiang 212013, China

ABSTRACT: In this study, a novel vehicle-mounted flywheel battery system is proposed, which can effectively balance the load capacity with margin, strong anti-interference, uncoupled magnetic circuit, and low energy consumption. The proposed new flywheel battery adopts multiple magnetic circuits, reducing the number of permanent magnets and the complexity of the magnetic circuit. It is worth mentioning that the proposed "side branch" radial/tilting shared magnetic circuit can realize the main bearing function of the flywheel weight, and the axial biased magnetic field is used to suspend the near "zero weight" flywheel, so that the flywheel can withstand a certain interference margin in the axial direction, and then improve the active disturbance rejection and effectively reduce the control loss. After optimization, the unique overall structure of the flywheel battery can significantly improve the overall performance of the flywheel battery. Finally, the stiffness, decoupling, and anti-interference experiments are carried out, and the experimental results show that the proposed flywheel battery has good performance.

1. INTRODUCTION

Flywheel battery system has great development potential in the field of new energy vehicles because of its advantages such as no pollution, high energy conversion efficiency, long cycle life, and insensitivity to temperature [1–3]. As a vehicle-mounted flywheel battery system is prone to instability due to the interference of vehicle operating conditions, the design of a magnetic support flywheel system directly determines whether the vehicle-mounted flywheel battery system can run safely and stably for a long time.

Unlike flywheel battery based on static foundation, its stability is easily affected by vehicle operating conditions [4, 5]. When the vehicle is in uphill and downhill conditions, the axial bearing capacity of the vehicle will be particularly prominent. Therefore, the design of axial magnetic bearing is particularly important. In [6], a novel vehicle-mounted magnetic suspension flywheel battery with a virtual inertial spindle is proposed. The axial magnetic bearing of the battery and the part of the flywheel are nested together, and the axial part adopts a double permanent magnet ring design, which can generate sufficient axial suspension force to just offset the gravity of the flywheel. In [7], an axial magnetic bearing is proposed, which utilizes an auxiliary air gap to make the electromagnetic magnetic circuit only overlap with the permanent magnetic circuit at the internal and external working air gaps. Although it avoids the electromagnetic magnetic circuit passing through the permanent magnet, it increases the axial air gap and reduces the magnetic flux density, thereby reducing the bearing capacity. For the magnetic suspension-flywheel system in [8], the axial biased flux generated by the permanent magnet is precisely calculated according to the weight of the flywheel and can only be controlled

in real time by the axial control coil when dealing with the axial disturbance. Therefore, the energy consumption of the system can be further improved. For the metal flywheel, it is very important to bear the weight of the flywheel with a certain disturbance margin in gravity direction (axial direction). The design of axial magnetic bearing directly affects the self-stability and energy consumption of the whole flywheel battery system.

In terms of active disturbance rejection performance, when the rotor of a traditional cylinder magnetic flywheel system is subjected to unbalanced response, the single magnetic direction of the cylinder air gap will make the mutual interference between magnetic circuits uncontrollable, thus affecting the stability performance of the whole flywheel system. The appearance of a spherical magnetic flywheel system enables the spherical air gap formed between stator and rotor to make the electromagnetic force always point towards the center of the sphere, realizing real-time adjustment, and thus weakening the unbalanced rotor response caused by gyroscope effect [9, 10]. However, spherical structure will also produce some leakage flux. Therefore, for different magnetic suspension-flywheel systems, the selection of spherical element size and quantitative analysis of radian are factors that need attention. In addition, the shape design of a flywheel should be closely matched with the magnetic bearing.

In terms of magnetic circuit design, it is difficult to balance the decoupling, loss, and integration of the overall structure. In the most common magnetic bearing topology, the static biased magnetic circuit of each degree of freedom is formed by its permanent magnets [11, 12], so the number of permanent magnets is large, which leads to the complexity of its magnetic circuit, and it is easy to lead to unnecessary superposition and weakening of its biased magnetic circuit. Some axial topol-
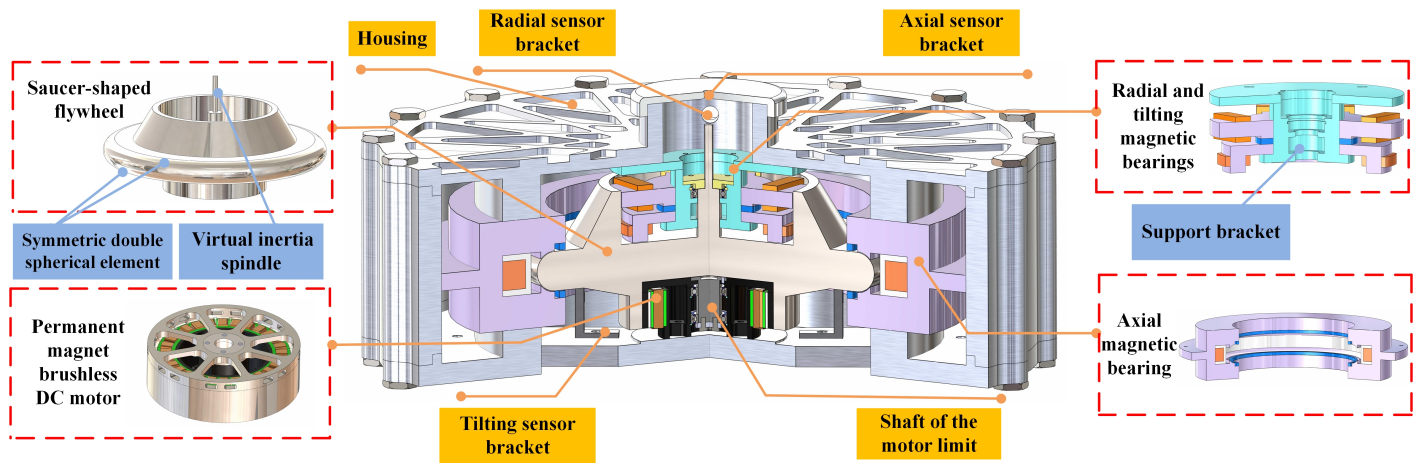
FIGURE 1. Overall structure of the novel vehicle-mounted magnetic suspension flywheel battery.

ogy structures effectively cut off the magnetic circuit by using the spatial height difference, but their magnetic suspension system is located on the upper and lower sides of the rotor, so the ultimate high integration is not achieved in the axial direction [13–16]. In [17], the radial part and axial part of the integral magnetic bearing are independent by a pair of radial stator arrangement, which can realize the decoupling design. However, this arrangement will reduce the axial integration level of the whole structure. By introducing a secondary air gap, the asymmetric three-pole magnetic bearing proposed in [18] can make the biased magnetic circuit and control magnetic circuit form channels respectively, effectively inhibiting the magnetic coupling, but causing a large magnetic leakage problem. In [19], its overall structure is unique, and its design is flat. However, due to its biased magnetic circuit and control magnetic circuit sharing, the coupling problem of several degrees of freedom is inevitably caused in this structure, which makes the control more difficult.

In this paper, a novel highly anti-interference and decoupled saucer-shaped vehicle-mounted magnetic suspension flywheel battery is proposed, which is significantly different from the traditional flywheel battery system. First, the overall topology and characteristics are introduced. Then the initial designs of flywheel and magnetic bearing system are carried out respectively, and then because the interaction between the two will directly affect the various characteristics of the flywheel battery system, further joint optimization design is carried out. Finally, the stiffness and performance tests are performed to verify the feasibility of the novel flywheel battery.

2. STRUCTURE DESIGN AND ANALYSIS

The proposed flywheel battery topology is shown in Fig. 1. It is particularly noteworthy that this prototype continues to adopt the classic concept of "virtual inertial spindle", but has undergone significant upgrades. Therefore, compared with traditional flywheel battery system with virtual inertial spindle, this prototype has higher axial integration, lower energy consump-

tion, better safety, stability, and energy storage performance. The details are as follows:

1. Higher axial integration: the concept of radial tiling of the axial stator is proposed. The radial axial dimension ratio of the structure is high, and the structure cleverly makes the radial part and tilting part share the biased magnetic circuit, which further reduces the axial dimension.

2. Higher stability: Since the outside of the flywheel is a symmetrical double sphere, the double electromagnetic force received by the flywheel during deflection always points to the center of the sphere and is symmetrical up and down, which has stronger anti-interference ability than the existing cylindrical surface and single sphere.

3. Higher safety: Compared with the existing virtual shaft flywheel battery, the flywheel proposed in this paper abandons the lower half of the column. The motor rotor and motor internal column are cleverly designed as a whole and fixed with the flywheel, and the motor stator and base are fixed together on the lower end cover. The double auxiliary bearing between the column and base of the motor can well realize the limit protection.

4. Higher energy storage performance: The "saucer-shaped" flywheel has a higher critical speed and a higher moment of inertia after optimization. The energy storage density will increase significantly, and the flywheel energy density is 17.8% higher than that before optimization.

2.1. Flywheel Design Analysis

As the energy storage part of the whole structure, flywheel shape design, material selection, and overall mass tradeoff are particularly important. If we simply pursue the energy storage density per unit mass, it will affect the energy storage density per unit volume of flywheel, and it is difficult to take advantage of the high power density of metal flywheel. In addition, if the flywheel mass is concentrated around the axis too much, large moment of inertia cannot be obtained. The flywheel design
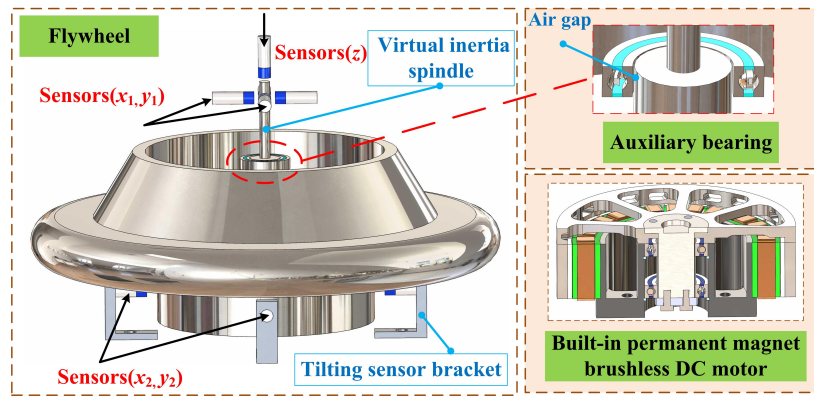
FIGURE 2. The protection and sensors installation of flywheel battery.

needs to consider the processing and assembly problems and achieve large inertia with small mass as far as possible within the allowable stress strength.

The expressions of flywheel energy storage E and energy storage density E_m are respectively:

$$E = \frac{1}{2} J \omega^2 \tag{1}$$

$$E_m = \frac{E}{m} = \frac{J \omega^2}{2m} \tag{2}$$

For the flywheel made of a single material, its energy storage density can be derived from the strength limit of the material and shape coefficient, and the specific expression is as follows:

$$E_m = \frac{K_s \sigma_{\max}}{\rho} \tag{3}$$

where E is the stored energy of the flywheel, E_m the energy storage density of the flywheel, ω the angular speed of the flywheel rotation, m the mass of the flywheel, J the moment of inertia of the flywheel, K_s the shape factor, $\sigma_{\max}$ the maximum permissible stress, and ρ the mass density.

The main parameters of the vehicle-mounted flywheel energy storage system are shown in Table 1.

TABLE 1. Main parameters of the vehicle-mounted flywheel energy storage.

Parameter	Value	Unit
Rotational speed	2500 20000	r/min
Stored energy	30	Wh
Flywheel weight	9.3	kg
Power of motor	2.5	kW
Input voltage	220	V
Output voltage	220	V

To increase the level of integration, the upper and lower sides of the flywheel are slotted to integrate the magnetic bearing, flywheel, and motor as one unit. The motor is embedded in the bottom of the flywheel. The flywheel and the outer rotor of the motor are assembled by interference fit. In order to monitor the position of the flywheel in real-time during operation, nine sensors are added at the bottom and top of the flywheel. The labeling and dimensions of the sensor with five degrees of freedom are illustrated in Fig. 2. The dimensions of radial two degrees of freedom are represented by x_1 and y_1, while the dimensions of tilting two degrees of freedom are denoted by x_2 and y_2. Additionally, z represents the dimensions of axial single degrees of freedom.

2.2. Magnetic Bearing Analysis

The structural explosion view of the proposed five-degree-of-freedom magnetic bearing and flywheel is shown in Fig. 3.
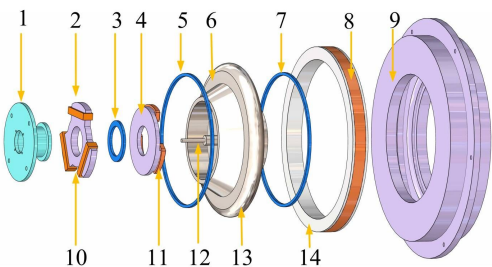

FIGURE 3. Explosion view of flywheel and magnetic bearing system. 1. Support frame assembly; 2. Radial stator; 3. Radial/tilting PM; 4. Tilting stator; 5. Axial upper PM; 6. Flywheel; 7. Axial lower PM; 8. Axial control coils; 9. Axial stator; 10. Radial control coils; 11. Tilting control coils; 12. Virtual inertia spindle; 13. Spherical element; 14. Axial coil brace.

The external double spherical axial magnetic bearing generates an axially biased magnetic field. The two groups of axial permanent magnets are symmetrically distributed up and down, and their magnetic fields can make the flywheel rotor stably suspended in the center position, which is not susceptible to small axial disturbances from the outside. Therefore, the axial interference force with a certain margin can be borne, so that the control energy consumption is lower. The bias flux generated by the radial and tilting common permanent magnet flows through three radial air gaps and three tilting air gaps, respectively. The control flux generated by the control coil is
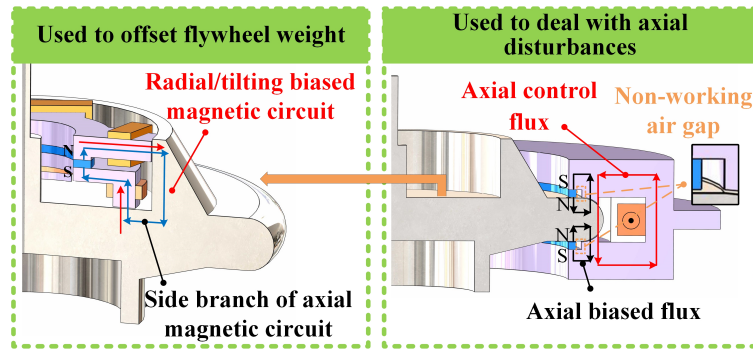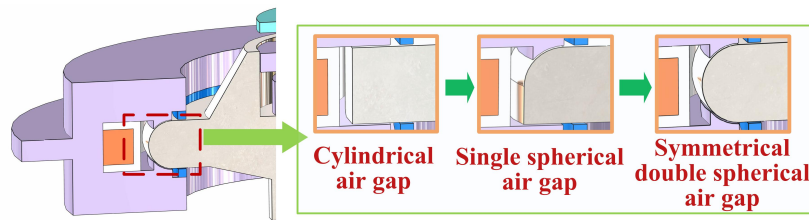
FIGURE 4. Axial magnetic circuit.

FIGURE 5. Comparison of different air gaps.

superimposed with the corresponding bias flux vector, which can realize the real-time adjustment control of the four degrees of freedom of the flywheel rotor radial and tilting.

In addition, only one permanent magnet is used to achieve the reuse of two biased magnetic circuits. The control fluxes of the radial and tilting parts are perpendicular to each other, thus enabling decoupling.

3. INITIAL OPTIMIZATION OF MAGNETIC BEARINGS

3.1. Analysis and Preliminary Optimization of Axial Magnetic Bearings

3.1.1. Axial Magnetic Bearing Analysis

In order to reduce the influence of external interference factors caused by vehicle running especially up-and-down turbulence, a new type of double spherical axial magnetic bearing is proposed for vehicle flywheel battery. In this structure, the flywheel suspension force is not provided by the traditional axially biased magnetic circuit, but by the tilting biased magnetic circuit. In addition, in axial magnetic bearings, the ingenious design of the "non-working air gap" effectively prevents the bias magnetic circuit from forming a self-loop, allowing the magnetic circuit to move in a predetermined direction, thus, the magnetic loss is reduced.

The axial control flux and biased flux are shown in Fig. 4. The magnetic circuit is also used as a "side branch of axial magnetic circuit" to carry flywheel weight, which is completely different from the traditional biased magnetic circuit. The "magnetic field" generating this force is not the "axial biased field" which can be superimposed with the axial control coil, but the real axial biased field is generated by axial permanent magnets

arranged symmetrically. Since the weight of the flywheel is already borne by the radial/tilting common permanent magnet, the weight of the flywheel is almost negligible in an axial biased magnetic field.

Different from the traditional cylindrical structure in Fig. 5, when the flywheel of the double spherical structure deflects, the suspension force will point to the center of the flywheel. Interference forces parallel to the radial direction of the flywheel can be eliminated; therefore, double spherical structure has a more stable up and down symmetry in the biased flux. As shown in Fig. 6, when the flywheel is offset 0.25 mm in the z direction, the magnetic pull generated by the unbalance of the ordinary cylindrical structure is 145 N, and the force generated by the single spherical structure is 133 N. However, the latest symmetrical double spherical magnetic bearing supported flywheel only needs 80 N controlling force to offset the unbalance magnetic pull caused by external interference. Therefore, the energy loss of the energized coil will be reduced. In addition, as the offset of the flywheel on the z-axis increases, the z-axis force gradually increases, while the x and y axis forces increase but are almost zero. It can be seen that the suspension force on the z axis is weakly coupled with the suspension force on the x and y axes. Therefore, the control complexity of the flywheel can be simplified in a certain small range.

3.1.2. The Preliminary Optimization of Axial Magnetic Bearings

After determining that the magnetic bearing in the axial part is a double sphere, it is necessary to study the influence of the diameter d and radian size a of this sphere on the entire axial part. The radian range of the double sphere is subject to geometric constraints, with the upper limit of 180 degrees. If the radian is too small, it will cause the curvature to be too small and close to
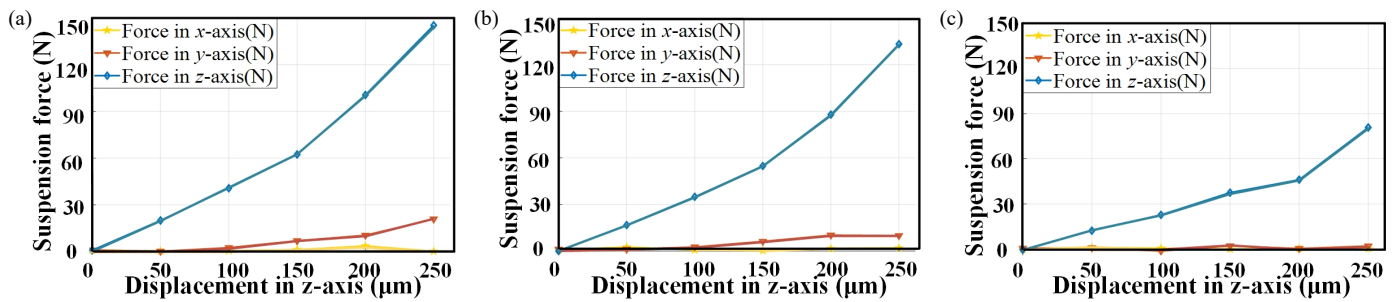
FIGURE 6. Force-displacement stiffness comparison diagram. (a) Cylindrical air gap structure. (b) Single spherical air gap structure. (c) Symmetrical double spherical air gap structure.
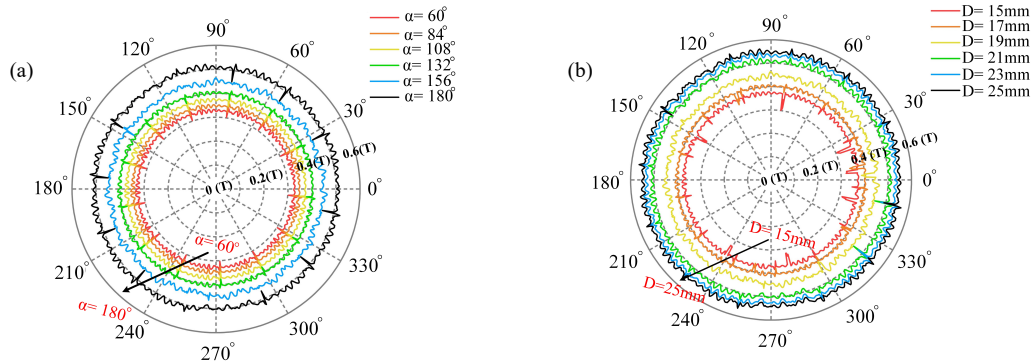

FIGURE 7. Axial air gap flux density distribution. (a) Influence of spherical radian on magnetic density of axial air gap. (b) Influence of spherical diameter on magnetic density of axial air gap.

the cylinder, so the angle is limited to 60 degrees. On the other hand, too large or too small spherical diameter will affect the overall topology. Therefore, the range of variables for spherical design is given below.

$$60° \leq \alpha \leq 180°; \quad 15\,\text{mm} \leq D \leq 25\,\text{mm} \qquad (4)$$

In order to more clearly see the influence of radian size on the magnetic density of the air gap, it is necessary to use the control variable method. The goal of spherical design is magnetic density B_a at axial air gap, and its range is as follows:

$$B_a \leq 0.6\,\text{T} \qquad (5)$$

Figure 7 shows the distribution of axial air-gap magnetic flux density. Because the axial magnetic bearing is a annular stator, there is a magnetic flux path in 360°. Fig. 7(a) is the optimization diagram of axial spherical radian a. In the optimization of radian a, the diameter d of the double spherical surface is fixed (the initial setting is 21 mm). As a increases from 60° to 180°, the axial air gap magnetic flux density of the magnetic bearing gradually increases from 0.32 T to 0.51 T, and the rule can be obtained as follows: The larger the radian size is, the greater the magnetic density of the air gap of the double spherical surface is, which can make full use of the permanent magnet material. Therefore, when the radian a is 180°, the magnetic flux density at the air gap $B_a = 0.51$ T can best meet the requirements, and the radian a is finally selected as 180°. Fig. 7(b) is the diameter d optimization diagram of the axial double spherical surface. In the optimization of D, a is fixed (radian a is chosen as 180°).

When d changes from 15 mm to 25 mm, the axial air gap magnetic flux density of the magnetic bearing gradually increases from 0.26 T to 0.55 T. It is observed that when the diameter d is small, the magnetic flux density at the air gap is small, and the magnetic flux fluctuation is large. The diameter size continues to increase; the flux density increases; and the fluctuation decreases. However, it is not possible to increase the diameter blindly, for two reasons: (1) Even if the diameter size continues to increase, the increase of magnetic density in the air gap is no longer obvious, but leads to material waste; (2) Considering the overall housing and space constraints, it is necessary to limit the axial diameter to a certain range. In summary, the final choice $D = 23$ mm.

3.2. Analysis and Preliminary Optimization of Radial and Tilting Magnetic Bearings

3.2.1. Radial and Tilting Magnetic Bearing Analysis

In order to ensure the compact structure and reasonable material utilization, the radial magnetic bearing and tilting magnetic bearing are integrated as a whole, and only one common permanent magnet is used. The radial/tilting flux path is shown in Fig. 8, and the magnetic circuit design is more ingenious than the traditional magnetic bearing. Moreover, there is no coupling between the overall magnetic circuit and the axial magnetic circuit mentioned above. The radial control principle is based on the working principle of AC magnetic bearings. The radial biased flux and control flux interact to adjust the radial position and achieve flywheel suspension. The tilting stator is
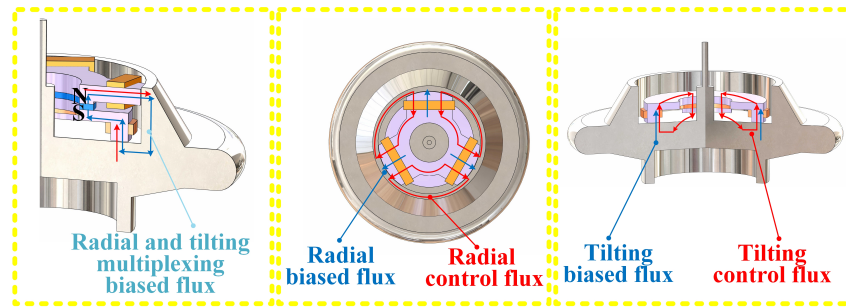
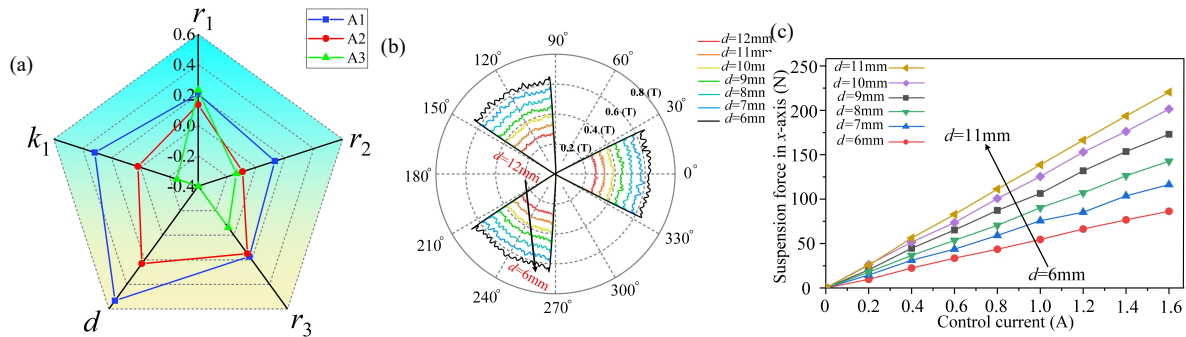**FIGURE 8**. Radial and tilting shared magnetic bearing.

FIGURE 9. Influence of stator parameters on stiffness and air gap magnetic density. (a) Sensitivity correlation of radial stator design variables; A1: Radial force-current stiffness; A2: Radial force-displacement stiffness; A3: Magnetic density of radial air gap. (b) Influence of radial stator pole thickness on magnetic density of radial air gap. (c) Influence of radial stator pole thickness on radial force-current stiffness.

in a sense like a "vertically extended"□ radial stator. The mechanism of action is similar to radial direction. When the flywheel is tilted, the angle can be adjusted to make the flywheel return to the initial position.

3.2.2. The Preliminary Optimization of Radial and Tilting Magnetic Bearings

In order to balance the selection of parameters and improve the performance of radial magnetic bearings, Fig. 9(a) shows the sensitivity of the three objectives of radial current stiffness A1, radial displacement stiffness A2, and radial air gap magnetic density A3 to the design variables (r_1, r_2, r_3, k_1, d). It can be seen that the current stiffness A1 is greatly affected by the radial stator pole thickness d and radial stator pole width k_1. The displacement stiffness A2 is not easily affected by design variables, so it will not be analyzed here considering the overall efficiency of parameter selection. The air gap flux density A3 is most affected by the radial stator pole thickness d.

However, it is considered that if the stator pole width k_1 is too large, the control coils on the three stator poles will collide with each other when winding, resulting in short circuit caused by the loss of insulating paint. Considering the distance between the coils, the stator radial pole width k_1 is determined to be 50 mm, and the influence of stator thickness d on current stiffness is analyzed emphatically. Therefore, when only the stator pole thickness d is optimized, other variables are initially set first. Considering the volume, mass of the flywheel and magnetic density characteristics of air gap, the initial value set

is as follows: The inner and outer radii of the stator, the outer radius of the stator pole are determined preliminarily, namely, r_1 is 27.5 mm, r_2 24 mm, r_3 53.5 mm, respectively. Considering the limited space inside the flywheel, it is necessary to limit the radial stator pole thickness within a certain range:

$$11\,\text{mm} \geq d \geq 6\,\text{mm} \qquad (6)$$

Figure 9(b) shows the optimization diagram of radial stator pole thickness d. As d changes from 6 mm to 12 mm, the radial air gap magnetic flux density of the magnetic bearing gradually decreases from 0.66 T to 0.28 T. Fig. 9(c) shows the influence of the radial stator pole thickness d on the radial force-current stiffness. As d changes from 6 mm to 11 mm, the current stiffness gradually increases. The maximum current stiffness was selected within the design specification of magnetic flux density (0.4–0.5 T), and the magnetic pole thickness d was finally selected to be 9 mm.

4. CO-OPTIMIZATION ANALYSIS

After determining the shape of the flywheel and the key size of the magnetic bearing, how to improve the overall performance of the flywheel, the joint optimization of the flywheel and magnetic bearing is particularly important.

When the flywheel speed is fixed, the flywheel structure design determines the moment of inertia and stress distribution. From formula (1) and (3), it can be seen that the energy storage density of the flywheel is directly proportional to the shape factor K_s of the flywheel and the stress required by the flywheel
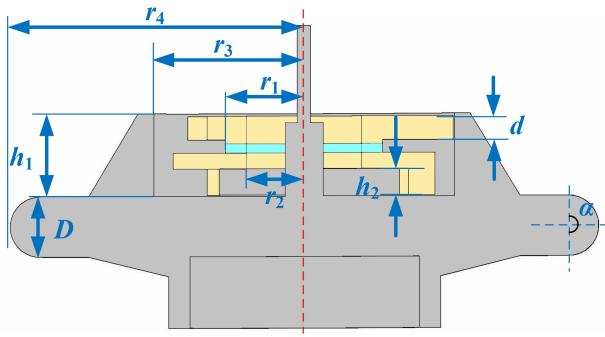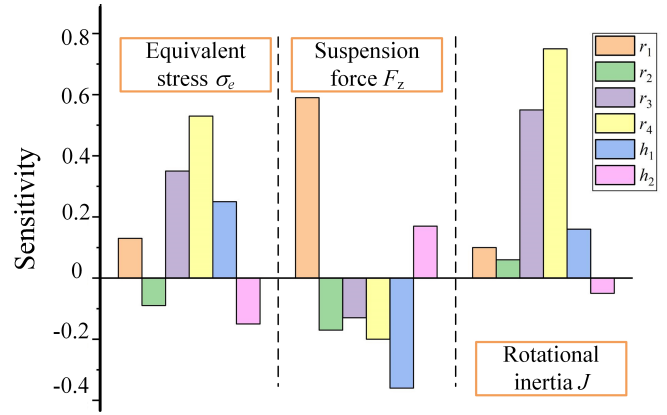
FIGURE 10. Optimal design variable.

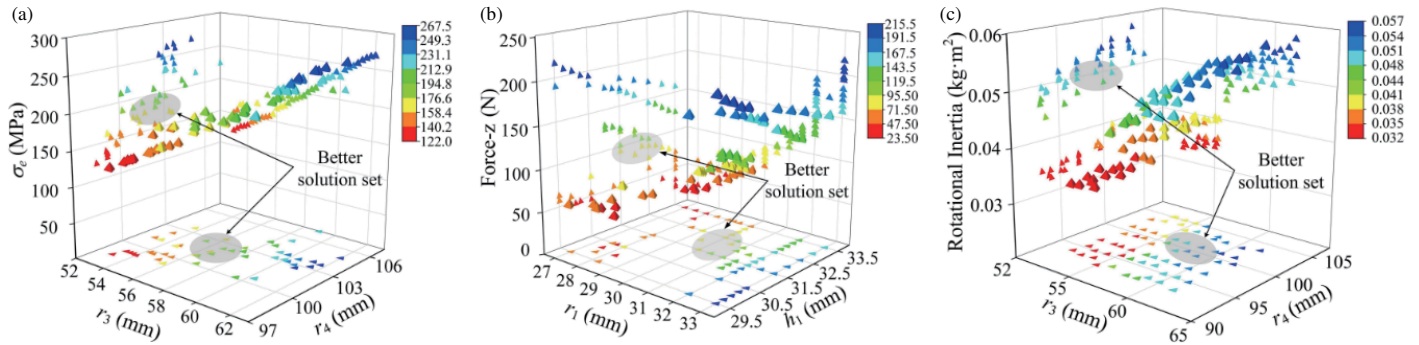**FIGURE 11**. Sensitivity analysis.

FIGURE 12. Better solution set after joint optimization.

material. Therefore, when the axial suspension force F_z and magnetic flux density B_0 at the working air gap are satisfied, rotational inertia J and equivalent stress σ_e of the flywheel are considered at the same time, and it is crucial to improve the energy storage density E_m of the flywheel.

The maximum allowable stress of the material used in the flywheel is about 300 MPa, and the maximum stress of the flywheel should be less than this value. It is worth noting that the stress utilization of the material should also be considered, so the maximum stress of the flywheel should not be too small. The criterion given here is that the maximum flywheel stress should not exceed two thirds of the maximum allowable stress of the material. Considering various factors, and the optimization objectives of this design are as follows:

$$\begin{cases} 103\,\text{N} \geq F_Z \geq 93\,\text{N}; & \dfrac{2}{3}\sigma_{\max} \geq \sigma_e \\ J \geq 0.04\,\text{kg}\cdot\text{m}^2; & 0.5\,\text{T} \geq B_0 \geq 0.4\,\text{T} \end{cases} \quad (7)$$

where σ_e is the equivalent stress of the flywheel, F_z the axial suspension force, and B_0 the biased magnetic density.

During the preliminary optimization of the magnetic bearing, the thickness of the radial stator pole d, spherical radian α, and spherical diameter D of the axial stator are obtained. Therefore, these parameters are not regarded as variables in the joint optimization, but are determined values. The dimensions closely related to the flywheel and magnetic bearing are selected as

variables, as shown in Fig. 10. The variables are as follows: radial stator outer radius r_1, inner radius r_2, the outer radius of stator pole r_3, the radius of the flywheel r_4, and the height of the groove in the upper part of the flywheel h_1, the pole length of tilting stator h_2.

On the other hand, to ensure that the overall topology model does not change, the design variables need to be limited to a certain range:

$$\begin{cases} 33\,\text{mm} \geq r_1 \geq 27\,\text{mm}; & 24\,\text{mm} \geq r_2 \geq 19\,\text{mm} \\ 65\,\text{mm} \geq r_3 \geq 52\,\text{mm}; & 106\,\text{mm} \geq r_4 \geq 90\,\text{mm} \\ 34\,\text{mm} \geq h_1 \geq 27\,\text{mm}; & 11\,\text{mm} \geq h_2 \geq 7\,\text{mm} \end{cases} \quad (8)$$

The sensitivity of design variables to objectives is shown in Fig. 11. In this paper, multi-objective genetic algorithm NSGA-II based on Pareto optimal solution is used for optimization. The final feasible point is shown in Fig. 12.

Through multi-objective optimization of flywheel and magnetic bearing, the optimal design variables are obtained, thus improving the overall performance of flywheel battery system. The specific parameters are shown in Table 2.

The three feasible points are all consistent with the target. Among them, E_m and J of feasible point 1 are the highest. Relative to the initial point, the energy storage density increases by 17.8%, and the moment of inertia increases by 18.6%. In addition, the equivalent stress of candidate point 1 material is also more utilized, reaching 195 MPa. Through the simulation, the
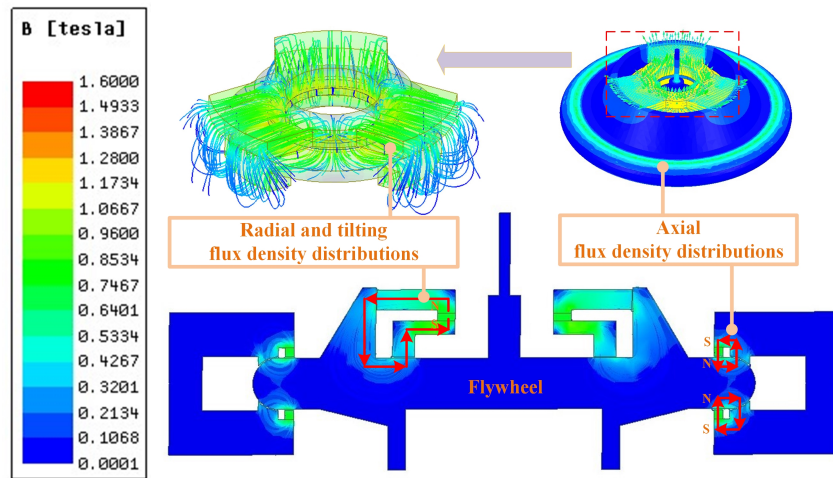
FIGURE 13. Overall biased flux distribution after optimization.

TABLE 2. Nominal parameters of the buck converter.

Parameters	Initial points	Feasible point		
		1	2	3
r_1 (mm)	27.5	30	31.5	29
r_2 (mm)	24	22	19.5	23
r_3 (mm)	53.5	57.5	59	62.5
r_4 (mm)	102.5	101	95	99
h_1 (mm)	27	31.5	33	29.5
h_2 (mm)	7.5	10	9.5	11
J (kg·m^2)	0.043	0.051	0.041	0.044
E_m (Wh/kg)	5.67	6.68	6.32	6.53
F_z (N)	79	98	102	93
σ_e (Mpa)	173	195	176	199
B_0 (T)	0.376	0.453	0.512	0.412

final design suspension force is 98 N, and the margin is about 5 N compared with the actual weight of the flywheel, which meets the practical requirements. The magnetic biased density of the radial pole and e tilting pole reaches 0.45 T, which satisfies the magnetic density characteristic of the air gap. The overall magnetic density distribution after optimization is shown in Fig. 13. It can be seen that the magnetic density distribution is uniform, and the direction of magnetic circuit accords with the theoretical result.

5. EXPERIMENTS

5.1. Platform and Control System

The prototype of the proposed saucer-shaped flywheel battery is shown in Fig. 14. The relevant experimental tests are based on a mobile vehicle experimental platform, as shown in Fig. 15. The platform is mainly composed of an electric vehicle, a flywheel battery system, a magnetic suspension control system, an auxiliary power distribution system, and a test system.

The block diagram of the 5-DOF magnetic control system is shown in Fig. 16. When the flywheel deviates from the equilibrium position due to external disturbance, the sensor obtains

the position feedback signal and sends the position deviation signal to the PID controller. PID controller uses force-current conversion module to convert deviation signal into active signal. Then the force signal is converted into the control current reference signal by the force-current conversion module. For radial and inclined magnetic bearings, a current-controlled voltage source inverter is used to obtain the excitation current in the three-phase coil. For axial magnetic bearings, an axial switching power amplifier is used to obtain the axial excitation current in the axial control coil. In addition, the control system adopts displacement current double closed-loop feedback control; the rotor can be suspended in the ideal balance position; and the real-time stability of the whole flywheel battery system can be improved.

5.2. Stiffness Performance Test

To study and verify the effectiveness of force-displacement and force-current transformation simulation models in the control system and the correctness of the previous stiffness theoretical analysis of the flywheel system, force-displacement stiffness and force- current stiffness tests are carried out. The usual sys-
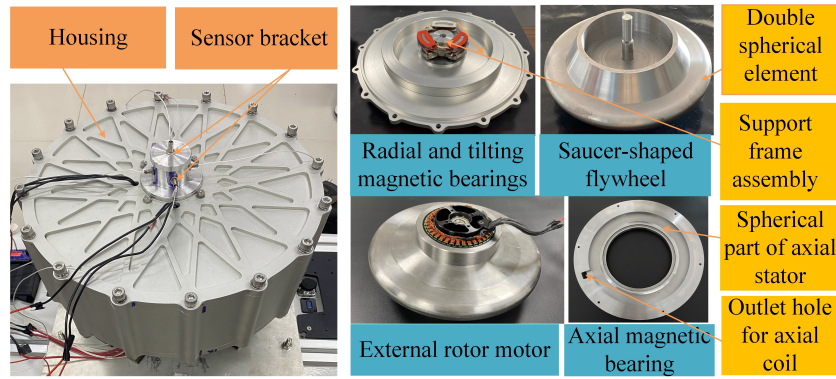
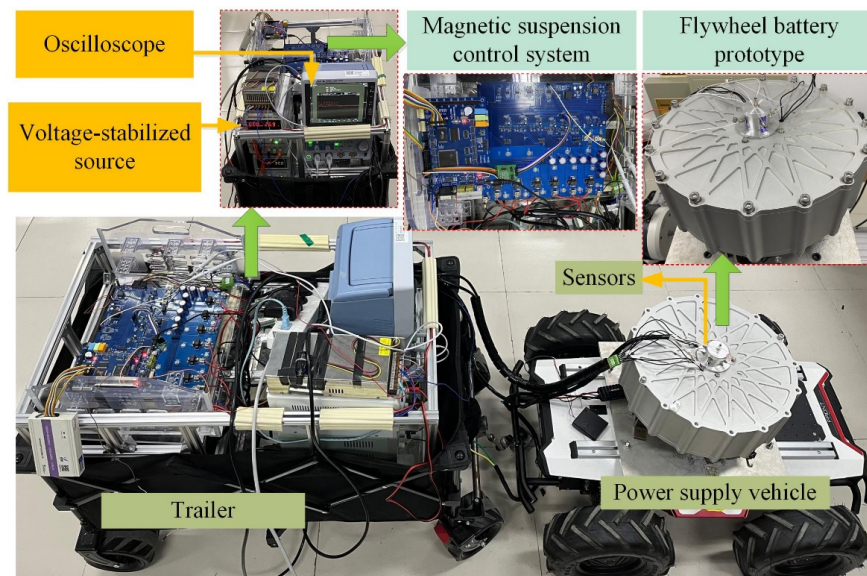**FIGURE 14**. Prototype of the saucer-shaped flywheel battery.

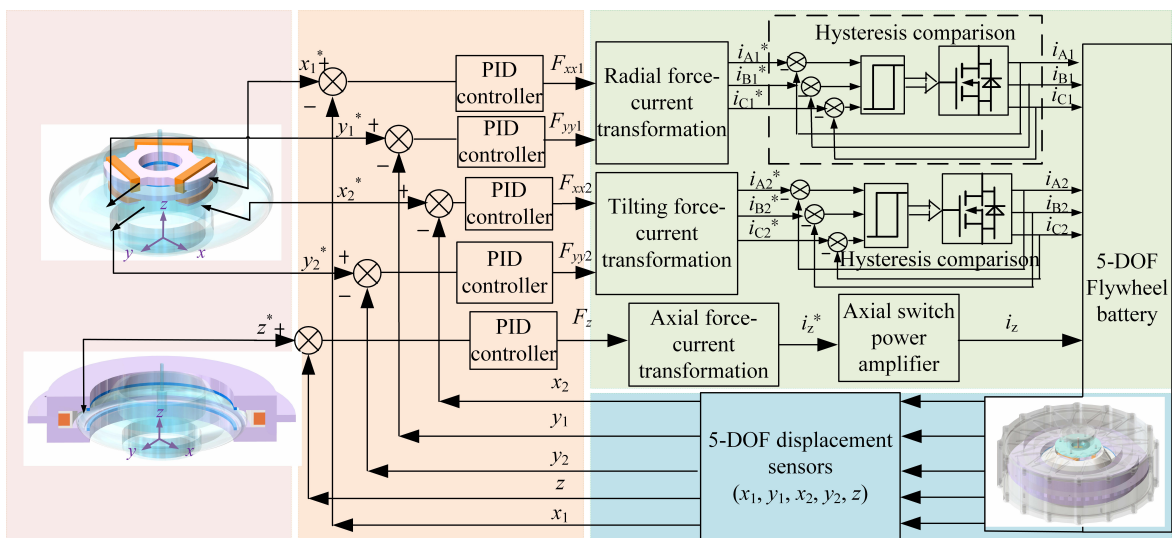**FIGURE 15**. Overall vehicle test platform.

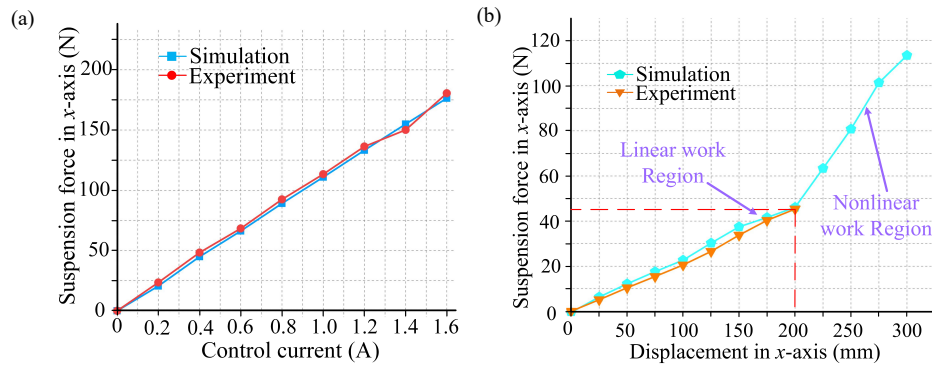**FIGURE 16**. The diagram of control system block.

FIGURE 17. Diagram of stiffness test. (a) Force-current stiffness in x-axis diagram. (b) Force-displacement stiffness in x-axis diagram.

tem studies various performances of the flywheel battery system under the influence of automobile working conditions, so in order to avoid the gyro effect brought by the high-speed flywheel to interfere with the analysis results, the stiffness and performance experiments are conducted at low speed.

Figure 17 shows the relationship between suspension force of radial magnetic bearing and the control current and the x-axis displacement. It can be observed that the experimental results are close to the simulation ones, which verifies the accuracy of models in control system. By comparing the simulated and experimental results, the auxiliary bearing of the structure limits the air gap in this study to less than 0.2 mm to ensure the linear area and precise control. From Fig. 17(a), it can be seen that when the offset reaches the limit value of 0.2 mm, only 0.34 A of current is required, indicating that the system has good anti-interference performance and effectively reduce the control loss.

5.3. Decoupling Experiment Test

Firstly, in order to verify the decoupling performance of the topological structure, a decoupling verification experiment is conducted. The experiment is conducted on the vehicle platform shown in Fig. 15. The experimental conditions are as follows: The vehicle suddenly decelerates in the x direction at 1 m/s^2. At this time, the displacement of each degree of freedom of the flywheel is shown in Fig. 18. As shown in Figs. 18(a) and (b), it can be seen that the vehicle-mounted flywheel battery is impacted in the x direction, so the flywheel is offset due to interference in the x direction. The flywheel x_1 has a maximum displacement offset of 0.059 mm. After adjusting 30 ms, the flywheel quickly became stable, and the peak displacement of flywheel x_1 dropped significantly to 0.029 mm. The maximum displacement offset of flywheel x_2 is 0.044 mm. After adjustment, the peak displacement of flywheel x_2 decreased significantly to 0.023 mm. The z displacement shown in Fig. 18(e) has almost no displacement. At the same time, it is found that the displacement in the y and z directions is almost unaffected by the disturbance in the x direction. The experimental results show that the design of the flywheel battery magnetic bearing system has good decoupling performance with multiple degrees of freedom.
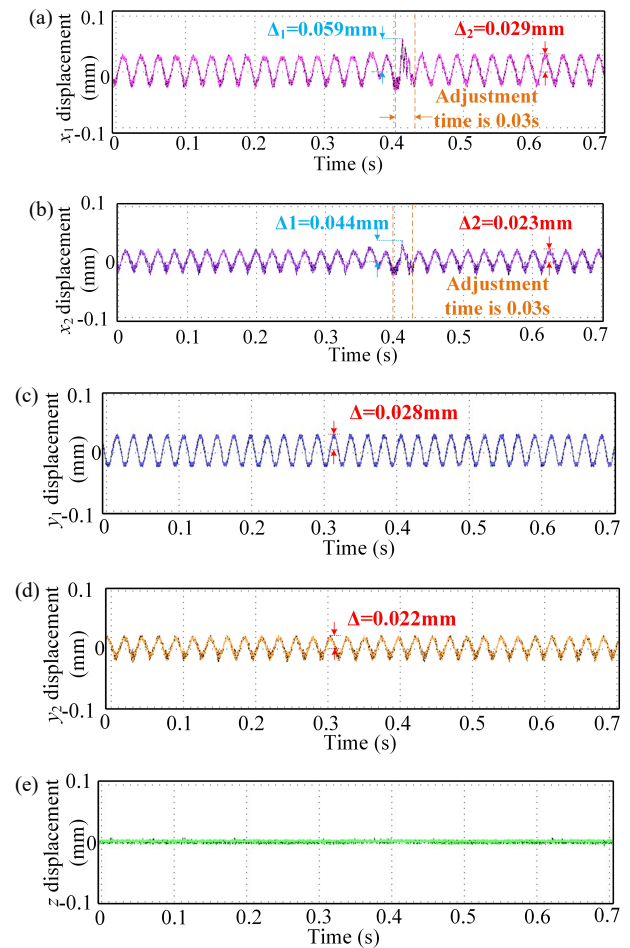

FIGURE 18. Decoupling experiment.

6. EXPERIMENTAL TEST OF ANTI-INTERFERENCE

Then, in order to test the anti-interference performance of the structure, the relevant experiments are done, and working conditions are as follows: the vehicle passes through the deceleration belt at constant speed, and the speed of the flywheel is 2500 r/min. Due to the side branch magnetic circuit of the structure, the flywheel has a certain anti-interference margin in the axial direction. As shown in Fig. 19, since both front and rear wheels of the overall flywheel battery have to pass through
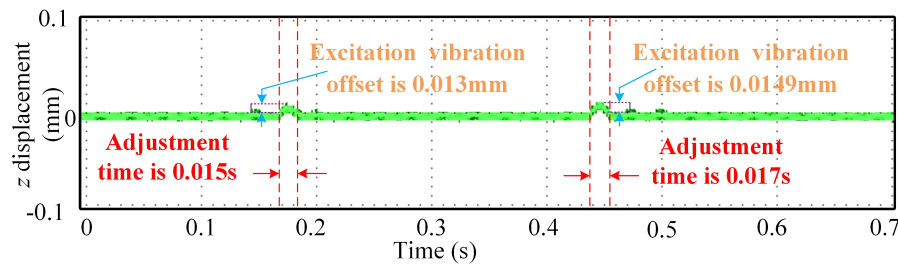
54

FIGURE 19. Axial anti-interference experiment.

the deceleration belt, it is equivalent to two excitations, and the flywheel immediately gets back to the initial position after two small displacements.

Finally, to test the anti-interference ability of structure, vehicle uphill experiments are conducted. Working conditions are as follows: Take a vehicle traveling in the y direction on a slope of 15 degrees as an example, and the speed of the flywheel is 2500 r/min. Fig. 20 is the flywheel trajectory chart at this time. The motion trajectory of the flywheel rotor when the vehicle is running smoothly on the slope is shown in Fig. 20, without showing the waveform of the process from flat road to uphill. As shown in Fig. 20(a) and Fig. 20(b), the flywheel is always near the balance position, indicating its strong anti-interference ability. As shown in Fig. 20(c), when the vehicle runs smoothly on a slope, its displacement is almost unaffected, and the operation is very smooth. It can be seen from the waveform that the decoupling performance of the topology structure has been verified, and it has high anti-interference ability.
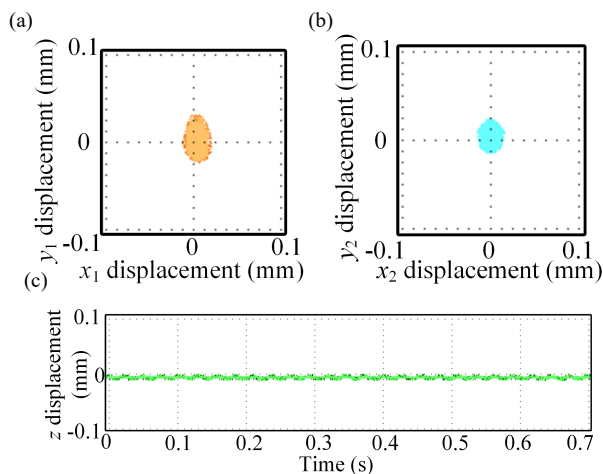

FIGURE 20. Flywheel motion trajectory.

7. CONCLUSION

In this article, a highly distinctive saucer-shaped magnetic suspension flywheel battery is designed and optimized. In this structure, the flywheel suspension force is not provided by the traditional axially biased magnetic circuit, but by the tilting biased magnetic circuit. Therefore, the axial interference force with a certain margin can be borne, so that the control energy consumption is lower. The magnetic circuit is a good trade-off between coupling and integration problems. Moreover, a saucer-shaped flywheel with spherical edges is proposed, which can significantly reduce the magnetic field imbalance interference force generated when the flywheel deflects or deflects because of different working conditions and energy consumption. Further, the combination of the saucer-shaped flywheel with spherical elements of the magnetic bearing and the optimization of the size and curvature of the sphere can make better use of the magnetic circuit. Finally, the stiffness test results verify the correctness of the analysis of magnetic bearing characteristics and prove that the flywheel battery is not susceptible to external interference. The good experimental results verify the decoupling and strong anti-interference of the topological structure. Therefore, the design concept of this prototype has been well proved.

REFERENCES

[1] Zhang, W. and Z. Wang, "Dual mode coordinated control of magnetic suspension flywheel battery based on vehicle driving conditions characteristics," *IEEE Transactions on Transportation Electrification*, Vol. 10, No. 1, 2124–2134, 2023.

[2] Adhikari, S. and R. Karki, "Integrated disturbance response modeling of wind-integrated power systems to quantify the operational reliability benefits of flywheel energy storage," *IEEE Transactions on Sustainable Energy*, Vol. 10, No. 3, 1152–1160, 2018.

[3] Bianchini, C., A. Torreggiani, D. David, and A. Bellini, "Design of motor/generator for flywheel batteries," *IEEE Transactions on Industrial Electronics*, Vol. 68, No. 10, 9675–9684, 2020.

[4] Wu, C., S. Lu, F. Xue, L. Jiang, and M. Chen, "Optimal sizing of onboard energy storage devices for electrified railway systems," *IEEE Transactions on Transportation Electrification*, Vol. 6, No. 3, 1301–1311, 2020.

[5] Sun, M., S. Zheng, K. Wang, and Y. Le, "Filter cross-feedback control for nutation mode of asymmetric rotors with gyroscopic effects," *IEEE/ASME Transactions on Mechatronics*, Vol. 25, No. 1, 248–258, 2019.

[6] Zhang, W., J. Wang, P. Zhu, and J. Yu, "A novel vehicle-mounted magnetic suspension flywheel battery with a virtual inertia spindle," *IEEE Transactions on Industrial Electronics*, Vol. 69, No. 6, 5973–5983, 2021.

[7] Zhu, Z., J. Zhu, H. Zhu, Y. Jiang, and M. Cheng, "A novel axial split phase bearingless switched reluctance machine for on-board flywheel battery," *IEEE Transactions on Vehicular Technology*, Vol. 70, No. 4, 3175–3186, 2021.

[8] Zhang, T., X. Ye, L. Mo, C. Zhang, Q. Lu, Z. Ding, and W. Ni, "Modeling and performance analysis on the five degrees of freedom slice hybrid magnetic bearing," *IEEE Transactions on Applied Superconductivity*, Vol. 29, No. 2, 1–5, 2018.

[9] Zhang, H., H. Zhu, and M. Wu, "Multi-objective parameter optimization-based design of six-pole radial hybrid magnetic bearing," *IEEE Journal of Emerging and Selected Topics in Power Electronics*, Vol. 10, No. 4, 4526–4535, 2021.

[10] Zhang, W., P. Zhu, J. Wang, and H. Zhu, "Stability control for a centripetal force type-magnetic bearing-rotor system based on golden frequency section point," *IEEE Transactions on Industrial Electronics*, Vol. 68, No. 12, 12 482–12 492, 2020.

[11] Zhang, T. and P. Bao, "Design of the six-pole hybrid magnetic bearing with separated magnetic circuit to generate symmetrical levitation force," *IEEE Transactions on Applied Superconductivity*, Vol. 31, No. 8, 1–4, 2021.

[12] Han, B., Y. Chen, S. Zheng, M. Li, and J. Xie, "Whirl mode suppression for AMB-rotor systems in control moment gyros considering significant gyroscopic effects," *IEEE Transactions on Industrial Electronics*, Vol. 68, No. 5, 4249–4258, 2020.

[13] Li, X., D. Dietz, J. An, N. Erd, Y. Gemeinder, and A. Binder, "Manufacture and testing of a magnetically suspended 0.5-kWh flywheel energy storage system," *IEEE Transactions on Industry Applications*, Vol. 58, No. 5, 6152–6162, 2022.

[14] Hutterer, M., D. Wimmer, and M. Schrödl, "Stabilization of a magnetically levitated rotor in the case of a defective radial actuator," *IEEE/ASME Transactions on Mechatronics*, Vol. 25, No. 6, 2599–2609, 2020.

[15] Ren, G.-P., Z. Chen, H.-T. Zhang, Y. Wu, H. Meng, D. Wu, and H. Ding, "Design of interval type-2 fuzzy controllers for active magnetic bearing systems," *IEEE/ASME Transactions on Mechatronics*, Vol. 25, No. 5, 2449–2459, 2020.

[16] Zhao, C., F. Sun, J. Jin, J. Tang, F. Xu, Q. Li, and K. Oka, "Analysis of quasi-zero power characteristic for a permanent magnetic levitation system with a variable flux path control mechanism," *IEEE/ASME Transactions on Mechatronics*, Vol. 26, No. 1, 437–447, 2020.

[17] Le, Q., "Design and analysis of a new five-degree-of-freedom dc hybrid magnetic bearing," *IEEE Transactions on Applied Superconductivity*, Vol. 31, No. 8, 1–4, 2021.

[18] Ren, X., M. Feng, and S. Chen, "Design method based on asymmetry factor of a novel three-pole magnetic bearing," *IEEE Transactions on Applied Superconductivity*, Vol. 31, No. 8, 1–4, 2021.

[19] Li, X., B. Anvari, A. Palazzolo, Z. Wang, and H. Toliyat, "A utility-scale flywheel energy storage system with a shaftless, hubless, high-strength steel rotor," *IEEE Transactions on Industrial Electronics*, Vol. 65, No. 8, 6667–6675, 2017.